Diagnosing Monthly Mean Boundary Layer Properties from Reanalysis Data Using a Bulk Boundary Layer Model

MAIKE AHLGRIMM AND DAVID A. RANDALL

Department of Atmospheric Science, Colorado State University, Fort Collins, Colorado

(Manuscript received 5 October 2004, in final form 2 August 2005)

ABSTRACT

The mixed-layer approach to modeling the planetary boundary layer (PBL) is particularly well suited to inversion-topped PBLs, such as the stratocumulus-topped boundary layer found off the west coast of America in the subtropical Pacific Ocean at northern and southern latitudes. However, a strong temperature inversion near 850 hPa (the trade wind inversion) is not confined to the stratocumulus regimes, but has been observed over most parts of the subtropical–tropical Pacific Ocean. In this paper, the authors test the ability of a simple bulk boundary layer model (BBLM) to diagnose entrainment velocity, cumulus mass flux, and surface latent heat flux from monthly mean reanalysis data. The PBL depth is estimated from Geoscience Laser Altimeter System data. The model is based on the conservation equations for mass, total water mixing ratio, and moist static energy.

The BBLM diagnoses entrainment velocities between 1 and 8 mm s^{-1} in the stratocumulus and trade wind regions, with increasing rates toward the west. Large cumulus mass fluxes (1.3–2 cm s^{-1}) mark the ITCZ and South Pacific convergence zone. Unreasonably large surface latent heat fluxes are diagnosed in regions where the vertical resolution of both model and input data are insufficient to represent the sharp gradients of moist conservable variables and winds across the PBL top. The results demonstrate that the potential exists to extract useful information about the large-scale structure of PBL physical processes by combining available observations with simple models.

1. Introduction

Following Stull (1988), the planetary boundary layer (PBL) can be defined as "that part of the troposphere that is directly influenced by the presence of the earth's surface, and it responds to surface forcings with a time scale of about an hour or less." Today, PBL processes are receiving increased attention because of their importance in the coupled atmosphere–ocean–land surface models that are used for seasonal forecasting and climate simulation. Errors in the parameterized surface fluxes are particularly dangerous in coupled models that simulate the circulations of both atmosphere and ocean because, in such models, errors in the surface fluxes lead to errors in the sea surface temperature (SST) and the simulated circulation of the ocean, which then feed back to produce further errors in the simulated circulation of the atmosphere. When the SST distribution is simply prescribed, errors in the surface fluxes are relatively harmless to the simulated atmospheric general circulation.

Despite the fundamental role of PBL processes in ocean–atmosphere–land surface interactions, our observations of the large-scale climatology of PBL parameters are very inadequate. There are major technical obstacles to obtaining the necessary measurements over sufficiently large regions of the earth. PBL parameters of particular interest include the following:

- the surface fluxes of sensible heat, latent heat, and momentum,
- the PBL depth,
- PBL cloudiness,
- the rate of turbulent entrainment across the PBL top, and
- the rate at which cumulus clouds remove mass from the PBL.

The importance of the surface fluxes is obvious. The PBL depth is critically important because it measures the PBL's holding capacity, such as for moisture, and also because it determines how rapidly the surface fluxes can modify the PBL's properties. PBL clouds strongly affect the earth's radiation budget (e.g., Norris

Corresponding author address: Maike Ahlgrimm, Dept. of Atmospheric Science, Colorado State University, Fort Collins, CO 80523.
E-mail: maike@atmos.colostate.edu

and Leovy 1994). The entrainment and cumulus mass fluxes are fundamental to the PBL's mass budget, as well as to its energy, moisture, and momentum budgets.

From a climatological perspective, the only PBL parameters listed above that are reasonably well observed at present are the surface momentum flux, which can be inferred from scatterometer data over the oceans (e.g., Chelton et al. 1990), and PBL cloudiness (e.g., Hahn and Warren 1999; Rossow and Schiffer 1999). Climatologies of the surface sensible and latent heat fluxes have been derived from in situ data (e.g., Woodruff et al. 1998) and satellite data (e.g., Chou et al. 2003), but large uncertainties remain.

Global observations of the PBL depth are now being retrieved via lidar from space. In a pioneering study, Winker et al. (1996) used a very limited sample of lidar data collected from the space shuttle to infer the PBL depth from aerosol backscatter gradients. Randall et al. (1998) used those data as well for comparison with the Colorado State University General Circulation Model. Much more extensive observations of the PBL depth retrieved by the satellite-based Geoscience Laser Altimeter System (GLAS; Zwally et al. 2002, 2005) are now becoming available. We use some of the GLAS data in this paper.

With considerable effort, the local PBL-top entrainment rate can be inferred from tracer measurements (Stevens et al. 2003a,b). Unfortunately, the large-scale distribution of the entrainment rate is virtually unknown. Recently, Wood and Bretherton (2004, hereafter WB04) combined satellite observations of cloud top temperature, sea surface temperature, and cloud liquid water path with National Centers for Environmental Prediction–National Center for Atmospheric Research (NCEP–NCAR) reanalysis data (Kistler et al. 2001). They estimated both the boundary layer depth and the entrainment rate, for the cloud-capped PBL. Their results will be discussed in more detail later on. Stevens et al. (2002) explored the effects of entrainment on the PBL winds over the tropical Pacific. They found that entrainment is quite important for the PBL's momentum budget, but a limitation of their study is that it lacked actual measurements of the entrainment rate, so the authors were forced to use specified values of the PBL depth and the entrainment rate.

The upward cumulus mass flux at the PBL top has been inferred diagnostically from data collected in a few field experiments (e.g., Yanai et al. 1973), but its climatological role in the PBL's large-scale budgets of mass, energy, water, and momentum has not yet been quantified.

In summary, among the PBL parameters listed above, four that are both poorly observed at present and unlikely to be well observed in the foreseeable future are the entrainment rate, the cumulus mass flux, and the surface latent and sensible heat fluxes. Our model can only diagnose three of these four, and we choose, somewhat arbitrarily, to focus on the latent heat flux. It is the dominant surface flux in our model region, and we are particularly interested in moist processes. A key goal of this study is to propose and demonstrate a method to determine entrainment rate, cumulus mass flux, and latent heat flux diagnostically, through the use of a simple PBL model, combined with analyses (or reanalyses) generated at a numerical weather prediction center, and the new lidar-derived PBL depth. In addition, exploration of the simple model, in connection with the data, provides insight into the physical relationships among PBL variables.

Section 2 discusses in more detail the tropical and subtropical marine PBL, as it relates to this work. Section 3 presents our bulk boundary layer model (BBLM). In section 4, we describe the reanalysis data and GLAS-derived PBL depth used as input for the BBLM. Results from the BBLM run and a discussion of the diagnosed fields is presented in section 5. In section 6, we summarize our work and offer some conclusions.

2. The PBL over the tropical Pacific Ocean

In this paper, we focus on three important PBL regimes that occur over the tropical Pacific. The stratocumulus regime, located over the cold upwelling ocean on the eastern boundaries of the Pacific basin, is characterized by a well-mixed PBL with a distinct top (e.g., Lilly 1968). Stratocumulus clouds form in the upper portion of the cool, humid layer that is in direct turbulent communication with the ocean. Moist static energy and total water (i.e., vapor plus liquid) mixing ratio are well mixed throughout the subcloud and cloud layers of the stratocumlus regime, but in the cloud layer the water vapor mixing ratio decreases upward (as the liquid water mixing ratio increases upward) and the dry static energy increases upward. Subtropical subsidence sets up a dry and warm free atmosphere overlying the cool and moist PBL. A strong temperature inversion separates the two air masses. We assume that the base of the temperature inversion is coincident with the PBL top. The distinction between the PBL and the free atmosphere is very sharp, well defined, and obvious.

The stratocumulus regime transitions into the trade cumulus regime over warmer waters (e.g., Bretherton and Pincus 1995). The trade cumulus regime is characterized by a well-mixed subcloud layer, topped by a weak inversion under shallow cumulus clouds, which are in turn capped by the usually much stronger trade

inversion. The fractional area covered by shallow cumuli can have a wide range. Examples of cloud fractions found during experiments are ~15% during the Barbados Oceanographic and Meteorological Experiment (BOMEX) (Siebesma et al. 2003), ~40% during Atlantic Trade Wind Experiment (ATEX) (Stevens et al. 2001) and between 40% and 70% in the Atlantic Stratocumulus Transition Experiment region (ASTEX) (Bretherton and Pincus 1995). We identify the combination of the subcloud layer and the trade wind cumulus layer as the PBL.

The deep convective regime is found over the warm pool of the western Pacific and Indian Oceans, and along the Intertropical Convergence Zone and South Pacific convergence zone. A well-mixed subcloud layer is capped by a weak inversion. The subcloud layer is conventionally identified with the PBL. The cumulus clouds above it can penetrate all the way to the upper troposphere. During times of suppressed convection, shallow cumuli or even stratocumulus layers can be found. These shallow cloud types can also coexist with the deep cumuli in the same large-scale region at the same time.

3. The bulk boundary layer model

In a mixed-layer model, conservative thermodynamic properties are assumed to be vertically well mixed throughout the PBL. More generally, a bulk boundary layer model represents the PBL's properties through their vertical averages, even though the profiles may not be well mixed. Our model variables, namely, total water mixing ratio and moist static energy, are sometimes, but not always, mixed throughout the full depth of the PBL. We assume that the vertically averaged total water mixing ratio and moist static energy can be used to characterize the PBL's moisture content and moist static energy, even when, as in the trade wind cumulus case, the PBL is not well mixed.

The BBLM is based on conservation equations for mass, total water mixing ratio, and moist static energy. Since we aim at diagnosing monthly mean fields, a steady state is assumed. All terms arising from temporal covariances are neglected. Finally, the density, ρ_0, is assumed to be constant. With these assumptions, the equations of the BBLM can be written as

$$\nabla \cdot (H\mathbf{v}_B) = w_E - w_C \tag{1}$$

$$\nabla \cdot (Hq_B\mathbf{v}_B) = w_E q_{B+} - w_C q_B + \frac{(F_q)_S}{\rho_0} \tag{2}$$

$$\nabla \cdot (Hh_B\mathbf{v}_B) = w_E h_{B+} - w_C h_B + \frac{(F_h)_S - \mathrm{RC}}{\rho_0}. \tag{3}$$

Here H is the boundary layer depth, $\mathbf{v}$ the horizontal wind, w_E the entrainment velocity, w_C the cumulus mass flux velocity across the PBL top, h the moist static energy, q total water mixing ratio, $(F_q)_S$ the surface flux of total water, $(F_h)_S$ the surface flux of moist static energy, and RC the radiative cooling of the air mass contained in the boundary layer (BL). Subscript B denotes vertically averaged, or bulk values, and subscript $B+$ refers to values just above the boundary layer top. In the horizontal advection terms of (2) and (3), the effects of vertical covariances of $\mathbf{v}$ with q and h have been neglected. No condensation and reevaporation terms have been included in the moisture equation, as we assume that they are equal and of opposite sign. This means that no precipitation is produced in the PBL. If no precipitation is falling into the PBL from above, assuming that condensation and reevaporation cancel each other implies that the surface precipitation rate is zero. If precipitation falls into the PBL, such as from deep convective clouds or anvil clouds, then our assumption implies that the same amount of precipitation impinges on the earth's surface.

The entrainment velocity, w_E, transports free-tropospheric air (with properties h_{B+} and q_{B+}) into the boundary layer. The cumulus mass flux velocity, w_C, removes air with properties q_B and h_B from the boundary layer through cumulus convection. The latter was first used by Arakawa and Schubert (1974). One of its consequences is that when we use (1) to derive the advective forms of (2) and (3), the cumulus terms drop out, leaving

$$H\mathbf{v}_B \cdot \nabla q_B = w_E(q_{B+} - q_B) + \frac{(F_q)_S}{\rho_0} \tag{4}$$

and

$$H\mathbf{v}_B \cdot \nabla h_B = w_E(h_{B+} - h_B) + \frac{(F_h)_S - \mathrm{RC}}{\rho_0}, \tag{5}$$

respectively. Since (1) is now the only equation in the set (1), (4), and (5) that contains w_C, we must use (1) to determine w_C. The convective mass flux is thus set by the BBLM's mass budget; that is,

$$w_C = w_E - \nabla \cdot (\mathbf{v}_B H). \tag{6}$$

Furthermore, we assume the PBL top to be coincident with the trade wind inversion, so the shallow cumulus clouds that are confined below the inversion do not contribute to w_C.

We neglect the effects of solar radiation for simplicity; the effects of terrestrial radiation are usually strongly dominant in the PBL. The vertically integrated radiative cooling rate, RC, is expressed in terms of the equivalent net longwave radiative flux difference (with

units of W m^{-2}) across the PBL, that is, between the PBL top and the surface. We determine RC at each grid point from the ECMWF radiative cooling profiles, for a given GLAS-derived PBL depth (see the appendix).

Note that the moist static energy flux at the surface is a linear combination of the dry static energy flux and the latent heat flux: $(F_h)_S = (F_s)_S + L(F_q)_S$. We can use Eqs. (4) and (5) to diagnose the entrainment velocity and the surface latent heat flux $L(F_q)_S$. It is useful to consider the special case in which the solution is determined locally, that is, in which all terms of (4), (5), and (6) that involve horizontal derivatives are negligible. Then Eqs. (4) and (5) can be solved for the entrainment velocity and latent heat flux:

$$\rho_0 w_E = \frac{(F_s)_S - \mathrm{RC}}{L(q_{B+} - q_B) - (h_{B+} - h_B)} \tag{7}$$

and

$$L(F_q)_S = L\,\frac{[(F_s)_S - \mathrm{RC}](q_{B+} - q_B)}{(h_{B+} - h_B) - L(q_{B+} - q_B)}. \tag{8}$$

Both the entrainment velocity and the surface latent heat flux depend on the net cooling of the layer (the difference of longwave radiative cooling and surface sensible heat flux). This is reasonable because a stronger cooling has to be balanced by a stronger latent heat flux to maintain the PBL at constant depth. In the absence of horizontal transport, the cumulus mass flux velocity equals the entrainment velocity. Equations (7)–(8) represent a local solution to which other solutions can be compared.

More generally, Eqs. (4) and (5) give

$$\rho_0 w_E = \frac{(F_s)_S - \mathrm{RC} - H[\rho_0 \mathbf{v}_B \cdot \nabla h_B - L(\rho_0 \mathbf{v}_B \cdot \nabla q_B)]}{L(q_{B+} - q_B) - (h_{B+} - h_B)}, \tag{9}$$

$$L(F_q)_S = L\,\frac{((F_s)_S - \mathrm{RC})(q_{B+} - q_B) - H[(\mathbf{v}_B \cdot \nabla h_B)(q_{B+} - q_B) - (h_{B+} - h_B)(\mathbf{v}_B \cdot \nabla q_B)]}{(h_{B+} - h_B) - L(q_{B+} - q_B)}. \tag{10}$$

First we use (9) and (10) to determine w_E and $(F_q)_S$. Then we substitute the resulting w_E into (6) to obtain w_C.

As explained in the next section, the BBLM makes use of gridded reanalysis data. The divergence operator in Eq. (6), that is, $\nabla \cdot (H\mathbf{v}_B)$, is approximated using simple centered finite differences on the grid.

4. Data

The BBLM takes most of its input from monthly mean ERA-40 gridded reanalysis data for October 2001. The PBL depth is obtained from lidar measurements between 26 September and 18 November 2003. October 2001 coincides with part of the *Ronald H. Brown*'s cruise in the east Pacific during the East Pacific Investigation of Climate (EPIC) (Bretherton et al. 2004). Reanalysis data is as yet unavailable for October 2003, the month for which we have GLAS-derived PBL data. Both October 2001 and 2003 occurred during near-neutral ENSO conditions. The monthly means for both years should be close enough to allow an evaluation of the method. In this study, we focus on the tropical and subtropical Pacific. The domain extends from 35°N to 30°S, 120°E to 70°W. This region covers a wide range of climate phenomena of interest, including marine stratocumulus decks, regions of strong convection in the ITCZ, SPCZ, the warm pool, and of course ENSO.

a. The Geoscience Laser Altimeter System data

The GLAS lidar on board the Ice, Cloud and Land Elevation Satellite (ICESat) pulses at 40-Hz frequency and 532-nm wavelength. The result is a backscatter profile every ~175 m horizontally with maximal vertical resolution of 76.8 m. For a better signal-to-noise ratio, eight consecutive profiles are averaged together before a search algorithm is applied to detect the PBL top. The boundary layer top is frequently marked by a sharp gradient in aerosol concentration. From the averaged backscatter profile, a background noise level is established. The profile is then searched from the ground up for a significant decrease in aerosol/cloud particle concentration. In the presence of optically thick boundary layer clouds, the signal is fully attenuated inside the cloud, and the first significant decrease in particle concentration from the ground up marks the cloud top. The lidar signal can also be attenuated in other optically thick clouds, such as deep convective towers, but easily penetrates optically thin clouds, such as cirrus. If no PBL top can be found in the lowest 6 km of the atmosphere, the search is abandoned. The quality of the PBL retrieval is determined from the ratio of the backscatter signal inside the PBL to the signal 500 m above the PBL, and assigned an integer value between 1 and 13 (larger values correspond to increasing confidence in the retrieval). The higher the particle concentration in

the PBL, the easier the PBL top is to find, and the higher the quality rating. Obviously, the quality rating will be significantly larger for cloudy PBLs compared to clear PBLs. In fact, only 10%–15% of all successful retrievals have a quality rating between 5 and 9. Most retrievals seem to fall into the cloudy (quality 10–13) or clear (quality 1–4) categories. (Palm et al. 2002)

The retrieval works very well in the stratocumulus regions and trade cumulus regions. Between 60% and 80% of all backscatter profiles yield a successful PBL-top retrieval, and 70% or more of those retrievals have a quality rating of 10 or better. The farther away from the stratocumulus regions, the more the quality rating decreases, an indication of fewer cloudy retrievals. The quality rating can be roughly translated into a vertical error estimate, with quality 2 corresponding to ~4 vertical bins (300 m), quality 5 ~ 2 vertical bins (150 m) and quality 10 ~ 1 vertical bin (76.8 m). This correspondence is still quite uncertain. A look at the standard deviation of the PBL depth shows the lowest values around 150 m in the stratocumulus region off the South American coast. Values up to 500 m can be found in the northeast Pacific stratocumulus region and extending along the equator from the coast to the date line. In the deep convective regions, the standard deviation varies widely between individual grid boxes, ranging from 500 to 1500 m.

In the deep convective regions, the signal is often fully attenuated in deep clouds. The number of successful retrievals is lower here (~20% of all backscatter profiles in the warm pool yield successful PBL-top retrievals). Effectively, periods of deep convective cloudiness that obscure the PBL are excluded from our average PBL depth, and we should expect the results to reflect this. Roughly 70% of the successful retrievals have a quality rating between 1 and 4. The majority of the remaining 30% have quality ratings between 10 and 13, supporting our interpretation that the quality rating reflects the difference between clear and cloudy boundary layers, as well as the retrieval quality. In this region, retrievals with good quality can possibly cause problems. If we interpret these retrievals to be cloudy, low (i.e., <3.5-km cloud top) clouds in this region cannot automatically be classified to be boundary layer clouds, and we may count clouds piercing the trade inversion as well. This poses a problem: in the stratocumulus regime and the transitional trade wind regime, where we can safely assume low clouds to be part of the boundary layer, retrievals with high quality rating increase our confidence in the PBL-top retrieval. In the deep convective regions, clear shots with low quality rating are more likely to represent the height of the true trade inversion, rather than the top of clouds that may or may not penetrate the inversion. Overall, our confidence in the accuracy of the GLAS-derived PBL depth is lower in the deep convective regions, in large part because fewer retrievals per grid box have been averaged in this region, but also because clear boundary layers produce a weaker signal and clouds that penetrate the trade inversion may erroneously be counted as boundary layer clouds.

We use all successful retrievals (all qualities ratings) with a PBL top less than 3500 m and calculate a 2.5° × 2.5° grid box average. PBL depths exceeding this limit are very unlikely to occur over the ocean and are probably mislabeled elevated aerosol or cloud layers. We compared the mean PBL depth and its standard deviation for October only and the full period of available data (26 September–18 November 2003) and found little difference in the mean PBL depth. One noticeable difference is that the lowest PBL depths off the Californian coast (~800 m) were found farther north in October than in September and November. This shift in location leads to a minimum in the all-data average of ~1000 m. The full period average turns out to be a bit smoother, particularly in the warm pool area where sampling errors are larger. We have therefore decided to use all available data.

The satellite is in a near-sun-synchronous orbit, and overpasses occur locally just after sunrise and just after sunset (around 0700 and 1400 local time). As the reanalysis data is daily mean, monthly mean data we average retrievals from both local morning and evening. The diurnal cycle of the cloud-topped marine boundary layer has been observed with an amplitude around 150–200 m (e.g., Bretherton et al. 2004; Ciesielski et al. 2001). The PBL is shallowest in the early afternoon and deepest in the early morning hours. GLAS samples the PBL depth between those extrema and is unlikely to bias its PBL depth estimate beyond the retrieval uncertainly.

The GLAS-derived mean PBL depth (Fig. 1) is lowest in the eastern ocean basins with a minimum just below 1000 m at the Californian coast. It increases toward the west up to around 2000 m in the South Pacific, and to ~1800 m around Hawaii. The PBL remains shallower along the equator, between 1250 and 1500 m. Similar PBL depths can be found in the warm pool area, though our confidence in the data is lowest here. Inversions with a base between 800 and 850 hPa have been observed both in the near-equatorial central Pacific (Kloesel and Albrecht 1989; Firestone and Albrecht 1986) as well as in the warm pool region during suppressed conditions (e.g., Johnson et al. 1993). Those observations correspond well to the PBL depths around 1500 m in these areas. Additional observations of the

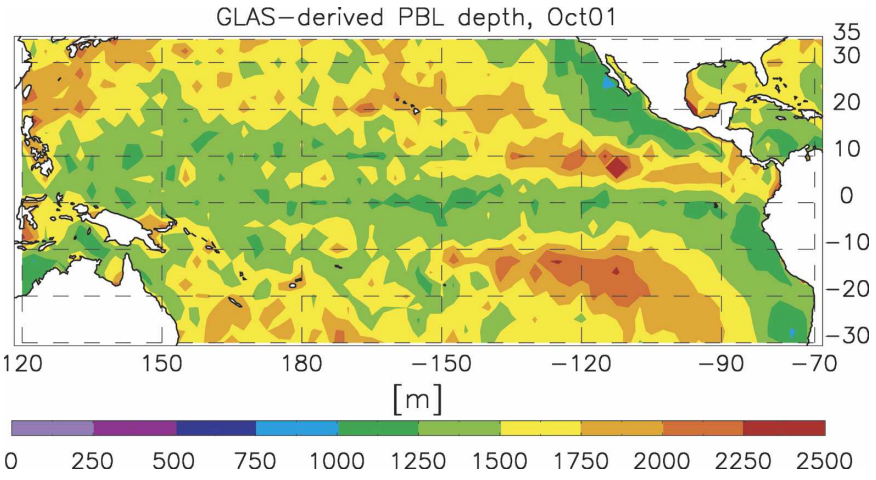

FIG. 1. GLAS-derived boundary layer depth, averaged from 26 Sep to 18 Nov 2003. Retrievals with PBL depths exceeding 3500 m have been excluded.

trade wind inversion are available from Neiburger et al. (1961) for the east Pacific between 30°N and 15°S, from Riehl et al. (1951) between the Californian coast and Hawaii, and from Garreaud et al. (2001) for the southeast Pacific from the coast of Chile along 27°S to 110°W. The observed inversion base height in Riehl et al. (1951) and Garreaud et al. (2001) generally agrees well with the GLAS PBL. Differences exist in the details, such as the inversion base observed by Garreaud et al. (2001), which dips down around 87°W, but then continues to increase westward. Such differences are to be expected when individual sonde measurements from one year are compared to the time mean GLAS data from another year. The South Pacific region covered by Neiburger et al. (1961) corresponds to regions of 1000–1500-m deep PBLs in the GLAS mean field. This is in general agreement again, though details differ. The North Pacific observations of Neiburger et al. (1961) show inversion bases lower than those in GLAS, by about 150 m. Overall, the PBL in GLAS tends to be somewhat deeper right next to the coast compared to these sonde-derived inversion estimates. During EPIC, inversion bases around 1000 m were found close to the Chilean coast, increasing toward the west to about 1250 m at 85°W, and decreasing again northward to the equator (Bretherton et al. 2004). The PBL is slightly deeper in the averaged GLAS data (~200 m), but changes in a similar manner from the Chilean coast to the equator.

Studies in which observations and simple boundary layer models are combined to calculate the PBL depth include Betts et al. (1992) and WB04. Both studies find PBL depths just below 1000 m at the Californian coast, increasing toward the west to ~1800 m. WB04 also consider the southeast Pacific region, where slightly larger values are found both at the coast and westward. The agreement of the GLAS-derived PBL depth with both of these studies is good. There may be a tendency for GLAS to overestimate the depth of the PBL. Further study of the GLAS data and comparison with in situ data obtained in 2003 are needed.

b. *ERA-40*

The ERA-40 reanalysis data (Uppala et al. 2005) are available on pressure surfaces and a 2.5° × 2.5° latitude–longitude grid. The moist static energy and total water mixing ratio are calculated on the 925 hPa (h_B, q_B) and 700 hPa (h_{B+}, q_{B+}) pressure surfaces from temperature, geopotential height, relative humidity, and the ERA-40 cloud water. The GLAS-derived PBL is quite deep, the PBL top lying between 925 and 775 hPa over most of the domain. Compared to the 1000-hPa level, we find that the 925-hPa level better represents the bulk layer values h_B, and q_B where the PBL is deep. This is a relaxation of the strict mixed layer assumption, for which h and q should be identical on all vertical levels inside the PBL. The horizontal advection terms of the BBLM, that is, $\mathbf{v}_B \cdot \nabla q_B$ and $\mathbf{v}_B \cdot \nabla h_B$, are evaluated on the 925-hPa level using finite differences on the reanalysis grid. Here h_B and q_B do not vary much inside the PBL, but we found significant wind shear in the PBL in the cold tongue area, which turns out to affect the BBLM results. This point will be discussed further in the results section.

PBL depth is available as a diagnostic field in the reanalysis. It is calculated using the bulk Richardson number method proposed by Troen and Mahrt (1986). Stepping upward through the atmosphere, a bulk Richardson number is calculated from the ground up from the difference in virtual dry static energy between the

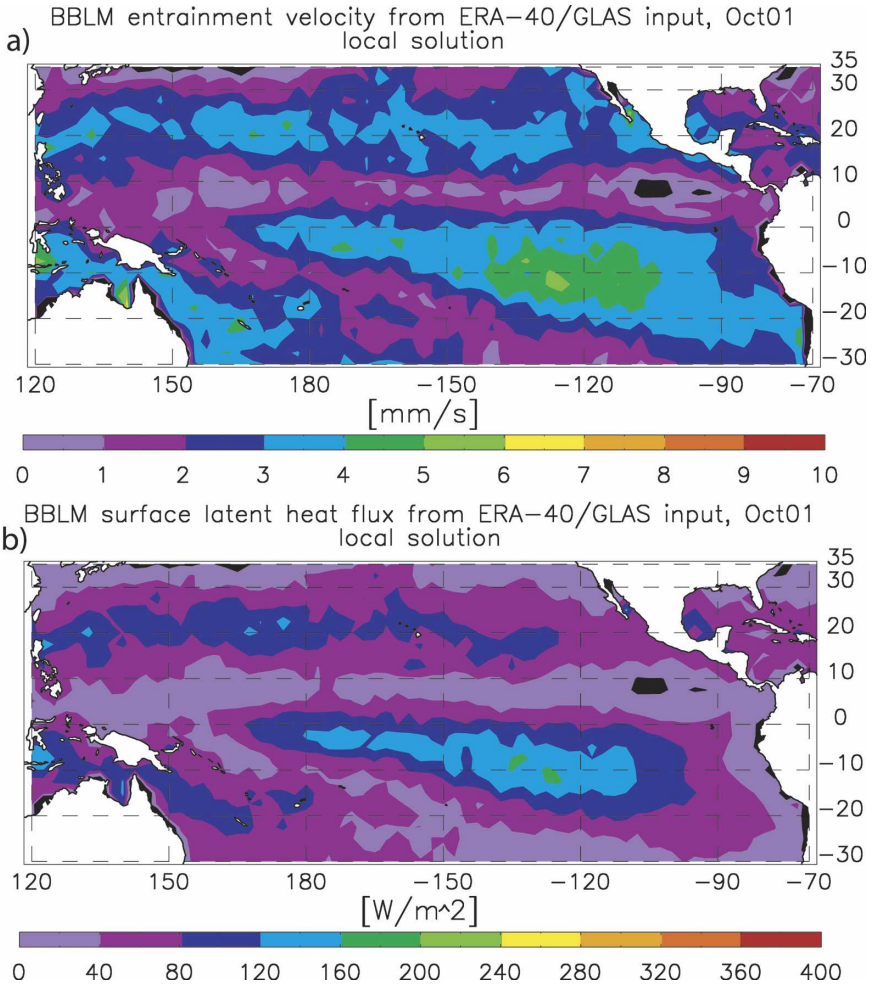

FIG. 2. Local solutions for (a) entrainment velocity and (b) surface latent heat flux.

current model level and the lowest model level. The PBL top is assigned where the bulk Richardson number reaches a critical value. The advantage of this method is that the PBL top can be diagnosed in stable and unstable situations, and in the presence and absence of a well-defined capping inversion. In contrast to the BBLM, the reanalysis PBL depth does not have to satisfy budget equations for mass, water, and moist static energy but is based on the local profile of virtual dry static energy. This quantity increases at the cloud base due to the increase in latent heat released from condensation of water vapor. In the presence of clouds, the bulk Richardson number method is therefore bound to diagnose the cloud base, rather than the cloud-top/trade inversion as in the BBLM. We should not expect the GLAS and ERA-40 PBL depths to coincide.

The surface evaporation rate and surface sensible heat flux are taken from the ERA-40 dataset as is and are used to calculate the surface moist static energy flux. The radiative cooling RC is the net longwave flux difference between the PBL top (from GLAS) and the surface, obtained from ERA-40 profiles (see the Appendix for a discussion.)

5. BBLM results with ERA-40 reanalysis data and GLAS PBL depth

In this section, we present results from the BBLM run with monthly mean ERA-40 data for October 2001 and GLAS PBL depth from October 2003.

Starting with the local solution (Fig. 2), the dependence of both entrainment velocity and surface latent heat flux on the local radiative cooling and surface sensible heat flux is quite apparent. Entrainment and latent heat flux are large where the difference (RC − $(F_s)_S$) is large, that is, where the PBL is strongly cooled. We note that the latent heat flux required to satisfy the local budget equations is very large, particularly in the

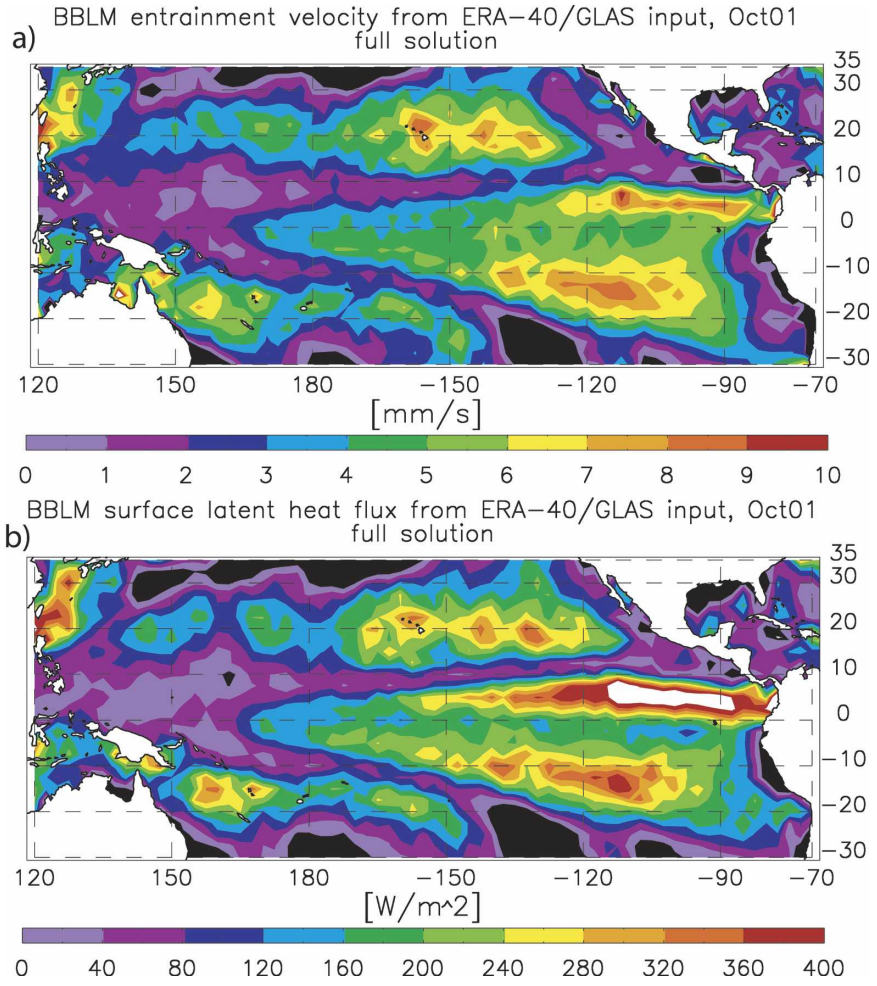

FIG. 3. Full solutions from BBLM for (a) entrainment velocity and (b) surface latent heat flux. White areas indicate above-scale values, black areas indicate below-scale values.

south-central Pacific. This is also the area with largest jumps of h and q across the PBL top.

Negative velocities can be seen along the South American coast. These stem from the poorly resolved contrast between low surface sensible heat flux over the ocean, and the large fluxes on land. Similarly, the advective contributions to the BBLM's budget equations are calculated as centered differences on the $2.5° \times 2.5°$ grid, so the gradients calculated across the coast are unreliable. The first grid points off the coast should be disregarded in the discussion of the diagnosed fields. We now present full solutions of the BBLM, including the effects of the nonlocal terms.

a. Entrainment velocity

Compared to the local solution, entrainment is enhanced in the central and southeast Pacific, the northeast Pacific, and in the cold tongue-to-ITCZ transition region (Fig. 3a). The increase in the entrainment rate is especially large in this transition region. Almost all of the 8 mm s^{-1} entrainment rate there is needed to balance cooling and drying by advection. Entrainment is also significantly enhanced in the northeast Pacific stratocumulus region. About two-thirds of the total entrainment rate is needed to balance advective cooling and drying. In contrast, the balance in the south-central Pacific area is mostly between the local radiative forcing and entrainment. This indicates that energy and water sources determining entrainment strength vary by region: In the cold tongue region and the northeast Pacific stratocumulus region, advection is an important contributor to the moist static energy and moisture budgets. East of the South American continent, local balances dominate.

WB04 found differences in entrainment strength between the Californian and the South American stratocumulus/trade wind regions as well. In their study, entrainment is found to be strongest close to the Cali-

fornian coast and decreasing away from the landmass, whereas the opposite occurs off the South American coast. WB04 argue that entrainment strength following the stratocumulus-to-cumulus transition depends sensitively on two opposing mechanisms: Moving away from the coast, the trade inversion weakens, which favors entrainment; on the other hand, the overall strength of turbulence decreases, opposing entrainment.

In the BBLM, entrainment in the southeast and central Pacific is primarily needed to balance the local radiative forcing $[(F_s)_S - \mathrm{RC}]$. While the BBLM does not explicitly represent feedback mechanisms, strong radiative cooling of the layer in combination with surface heating would be expected to favor a regime with enhanced turbulence, thus favoring stronger entrainment. Apparently, stronger radiatively driven turbulence and a weaker inversion act together, resulting in overall stronger entrainment west of the South American coast. In the ERA-40 reanalysis data, the surface sensible heat flux $[(F_T)_S \cong (F_s)_S]$, as well as the radiative cooling (Fig. A3) have their maximum away from the South American coast.

North of the ITCZ, the BBLM diagnoses entrainment rates around 3 mm s^{-1} close to the coast, decreasing only slightly toward the west before increasing to $\sim$7 mm s^{-1} halfway between the coast and Hawaii. While the entrainment rates are of comparable magnitude, the BBLM does not show the strongest entrainment rate close to coast, as in WB04. The BBLM results along the coast may be tainted by errors due to the numerical differences calculated on the grid, as discussed above. Additional factors that may contribute to the discrepancies near the Californian coast are 1) the underestimation of the stratocumulus frequency of occurrence in the ERA-40 (e.g., Chevallier et al. 2001) and 2) a potential bias in the WB04 estimate of the boundary layer depth and entrainment velocity, which is only valid for cloudy conditions.

The lack of stratocumulus clouds along the Californian coast in the ERA-40 data can likely be linked to the relatively low radiative cooling found in the ERA-40 data in this region (Fig. A3), and may therefore contribute to the lower entrainment rates in the BBLM. In the GLAS data, we find that 20%–30% of the retrievals along, and south of, the coast of Baja California detect a PBL top with weak optical signal (quality rating 1–4); that is, the boundary layer is likely clear. The retrieved boundary layer depth averaged for these cases is approximately 200 m shallower than the average depth for cloudy conditions (quality rating 10–13). While the PBL depth used in the BBLM includes both clear and cloudy conditions, WB04's estimate of PBL depth (and therefore entrainment rate) is biased toward cloudy conditions. This bias could possibly contribute to the difference between the BBLM and the WB04 estimate of the entrainment rate. Since the local radiative forcing in the BBLM is weaker in the northeast Pacific compared to the southeast Pacific, the WB04 balance between weakening inversion and reduced turbulence may well apply here.

In the Second Dynamics and Chemistry of Marine Stratocumulus (DYCOMS-II) study region (around 31°N, 122°W) entrainment velocities between $\sim$2 and 7 mm s^{-1} were measured using various tracers (Faloona et al. 2005). Overall, the magnitude of the entrainment rates diagnosed by the BBLM agree fairly well with those of both WB04 and DYCOMS.

The negative entrainment rates at the north and south boundary of the domain mark the latitudes at which midlatitudinal disturbances become important in the monthly mean input data. This is the true limit of our domain, as we can not expect the BBLM to work in those conditions.

b. Surface latent heat flux

The full solution for the latent heat flux yields even larger values than the local solution, particularly where the cold tongue transitions into the ITCZ (Fig. 3b). Here the advective contributions to the budgets are huge. At its largest, the term $H\mathbf{v}_B \cdot \nabla h_B$ in the moist static energy equation contributes on the order of 450 W m^{-1} to the budget. We have multiplied the moisture equation by the latent heat of condensation [to convert to units of W m^{-2}; Eq. (11)] and listed the contributions to the budget equation for two individual grid points and averages for the two parts of the domain corresponding to 500 hPa upward and downward velocity (Table 1). Similarly, the contributions to (12) are listed in Table 2. To obtain (12), we first subtracted (11) from the moist static energy equation to get the dry static energy budget. Separation of the moisture and heat budget facilitates an easier interpretation:

$$0 = -(LH\rho_0 \mathbf{v}_B \cdot \nabla q_B) + \rho_0 w_E L(q_{B+} - q_B) + L(F_q)_S \tag{11}$$

$$0 = -(H\rho_0 \mathbf{v}_B \cdot \nabla s_B) + \rho_0 w_E(s_{B+} - s_B) + (F_s)_S - \mathrm{RC}. \tag{12}$$

From the cold tongue into the ITCZ, a large temperature and humidity gradient exists nearly parallel to the equator. The meridional winds crossing the equator at these longitudes lead to large transports. Significant wind shear can exist over the cold tongue (McGauley et al. 2004). Since both advection and the entrainment term contribute negatively to the budget in Eq. (11),

TABLE 1. Latent heat budget of the BBLM and from de Szoeke et al. (2005); units: W m^{-2}.

	$-\rho_0 LH\mathbf{v}_B \cdot \nabla q_B$	$\rho_0 L w_E(q_{B+} - q_B)$	$L(F_q)_S$
ω (500 hPa) > 0	−61	−98	159
ω (500 hPa) < 0	−25	−53	78
0°, 95°W	−102	−93	195
2.5°N, 95°W	−278	−95	373
de Szoeke et al. (2005) 0.7°N, 95°W	−74	−39	113
de Szoeke et al. (2005) 2.3°N, 95°W	−158	−12	170

balance must be maintained through surface evaporation. We do not claim that the latent heat flux thus diagnosed is realistic. Similarly, warming through the prescribed sensible heat flux and through entrainment is balanced by radiative cooling and advection in Eq. (12).

The transition from the cold tongue into the ITCZ along 95°W has been studied during EPIC. de Szoeke et al. (2005) estimate the heat and moisture budget in this region from a multitude of measurements, including ship, aircraft, satellite, and moored instrument platforms. An estimate of the budget contributions for September–October 2001 for the locations (0.7°N, 95°W) and (2.3°N, 95°W) shows that the BBLM seriously overestimates the moisture and dry static energy advection in this area (see Tables 1 and 2); the PBL-top jumps of moisture and moist static energy are overestimated as well. The entrained air over the cold tongue is observed to be quite moist (specific humidity jump across the inversion on the order of 1 g kg^{-1}; de Szoeke et al. 2005), though only in a very shallow layer above the PBL top. This air is part of a shallow northerly return flow carrying moist air out of the ITCZ just above the southerly boundary layer inflow into the ITCZ (Zhang et al. 2004; McGauley et al. 2004). The BBLM's coarse estimate of the PBL-top jump results in a much larger value, as the free-tropospheric value of total water is taken from the 700-hPa level rather than from just above the PBL top. Even if we pick the closest pressure levels straddling the GLAS PBL depth, the jumps are too large. The vertical resolution of the input data may be too coarse to capture the complicated structures in the cold tongue to ITCZ transition zone.

It is obvious from the tables that the estimates of radiative cooling and surface sensible heat flux differ between the BBLM and the de Szoeke study. To obtain more meaningful values for comparison, we force the BBLM with the de Szoeke estimates for radiative cooling, sensible heat flux, PBL depth [determined by visual inspection of relative humidity and potential temperature cross sections (Fig. 7 of de Szoeke et al. 2005) to be ~1 km and ~1.2 km at 0° and 2.5°N, respectively] and PBL-top jumps [$(q_{B+} - q_B) = 1$ g kg^{-1} and $(s_{B+} - s_B)/c_p = 2.6$ K]. Not surprisingly, advection and entrainment in Eq. (12) now balance approximately, though both terms have about 1.5 times the magnitude of the de Szoeke terms (Table 3). We can conclude that the advection $\rho_0 \mathbf{v}_B \cdot \nabla s_B$ prescribed from ERA-40 is larger than the values used in de Szoeke et al. (2005). Entrainment rates of 1.4 cm s^{-1} (0°, 95°W) and 2.1 cm s^{-1} (0°, 95°W) are now needed to balance the budget. In Eq. (11), the BBLM advection terms remains ~1.2 times larger than in the de Szoeke estimate, balanced by a surface latent heat flux and entrainment term both in excess of the de Szoeke estimates (Table 4).

Another source for error is the assumption that no precipitation originates in the PBL. This assumption may be particularly unsuitable for the south side of the ITCZ. A large-eddy simulation (LES) study by de Szoeke and Bretherton (2004) simulating the cold tongue to ITCZ transition shows small (order of 10 W m^{-2}) but noticeable contributions to the PBL's liquid water potential temperature budget between the equator and 4°N due to precipitation originating in the PBL. The contribution to the budget over the cold tongue is negligible. The simulation does not extend

TABLE 2. Dry static energy budget ($s = c_pT + gz$) of the BBLM and heat budget (c_pT) from de Szoeke et al. (2005); units: W m^{-2}.

	$-\rho_0 H\mathbf{v}_B \cdot \nabla s_B$	$\rho_0 w_E(s_{B+} - s_B)$	$(F_s)_S$	−RC
ω (500 hPa) > 0	−20	68	13	−60
ω (500 hPa) < 0	−4	30	12	−38
0°, 95°W	−54	107	10	−63
2.5°N, 95°W	−88	99	30	−41
de Szoeke et al. (2005) 0.7°N, 95°W	−30	27	22	−20
de Szoeke et al. (2005) 2.3°N, 95°W	−47	40	33	−26

TABLE 3. Dry static energy budget ($s = c_pT + gz$) of the BBLM forced with de Szoeke et al. (2005) estimates of RC, $(F_s)_S$, H and $\rho_0(s_{B+} - s_B)$; units: W m^{-2}.

	$-\rho_0 H\mathbf{v}_B \cdot \nabla s_B$	$\rho_0 w_E(s_{B+} - s_B)$	$(F_s)_S$	$-RC$
0°, 95°W	−45	43	22	−20
2.5°N, 95°W	−70	63	33	−26

beyond 4°N, though. More significant contributions farther north are possible. Shallow cloud tops that might produce precipitation in the PBL are, in fact, detected by GLAS at the southern edge of the ITCZ (not shown here).

For completeness, we calculated the covariance $\overline{\mathbf{v}'_B \cdot \nabla q'_B}$ and $\overline{\mathbf{v}'_B \cdot \nabla h'_B}$ from the 6-hourly reanalysis data (Ahlgrimm 2004), but found their contribution to the budget equations small. The magnitude of other covariances, such as $\overline{w'_E(q'_{B+} - q'_B)}$ and $\overline{H'(\mathbf{v}'_B \cdot \nabla q'_B)}$ (and the equivalent terms for the moist static energy), remains unknown. A diurnal cycle in the stratocumulus topped PBL depth has been observed during EPIC (e.g., Bretherton et al. 2004), which may also be reflected in the corresponding entrainment velocity. It is possible that these covariances would contribute in a significant manner to the BBLM's budget equations, at least in certain areas.

c. Cumulus mass flux

The cumulus mass flux velocity, calculated as the residual term in Eq. (1), is shown in Fig. 4. Maximum values appear in the ITCZ (~2 cm s^{-1}) and SPCZ (~1.5 cm s^{-1}) east of the date line. In the warm pool area the mass flux varies, with velocities around 0.5 cm s^{-1}. Small positive and negative values dominate in the northeast, southeast, and central Pacific. Ideally, the cumulus mass flux should be zero where no convective clouds pierce the PBL top, which we have identified as the trade inversion. Midlevel and deep cumuli should contribute to a positive cumulus mass flux; shallow cumuli contained underneath the trade inversion should not. Clearly, negative mass fluxes are wrong. However, neither field used to calculate w_C, namely the entrainment velocity and PBL depth, is particularly smooth, and steep gradients in H translate into large changes in w_C. The mass flux in the warm pool might be interpreted as the grid box mean of clear shots (no mass flux) and cloudy shots penetrating the trade inversion (positive mass flux). As mentioned in the data section, GLAS apparently detects a mixture of clear and cloudy shots in the warm pool area. A small convective cloud that is strong enough to pierce the inversion, yet shallow enough to be mistaken as a boundary layer cloud, might contribute to a small mass flux. A similar argument can be made for the ITCZ and SPCZ. When only low quality (1–4) retrievals are averaged, the PBL depth decreases by about 200 m in the ITCZ. This alone does not modify the mass flux much. We can rewrite Eq. (1) as

$$H\nabla \cdot \mathbf{v}_B + \mathbf{v}_B \cdot \nabla H = w_E - w_C. \tag{13}$$

The left-hand side is clearly dominated by the wind divergence, which is particularly strong (and negative, i.e., convergent) in the ITCZ and SPCZ east of the date line. While our model equations for entrainment and the latent heat flux are dominated by the moisture and moist static energy budget, the equation for the cumulus mass flux is simply the mass budget. Even though the PBL-depth input field excludes scenes of deep convection, mass has to be removed from the PBL in regions with strong convergence, namely the ITCZ and SPCZ. In the BBLM, deep convection is primarily mass driven in these areas, while the (weaker) mass flux in the warm pool is determined both by weak convergence and the thermodynamic budget.

Comparison of the mass flux derived here with other studies is difficult for a variety of reasons, some of which have been touched on in the previous paragraphs. The BBLM's cumulus mass flux excludes contributions from shallow cumuli and is averaged in time and space, including clear as well as cloudy conditions. Despite the obvious difficulties in diagnosing this field, the general magnitude of the cumulus mass flux is comparable to the mass flux derived in other studies. For example, the average cloud-base mass flux derived in Yanai et al. (1973) for the warm pool region is ~8 hPa h^{-1}, which corresponds roughly to a 2 cm s^{-1} mass flux velocity (using the hydrostatic equation for conversion).

TABLE 4. Latent heat budget of the BBLM forced with de Szoeke et al. (2005) estimates of, H and $(q_{B+} - q_B)$; units: W m^{-2}.

	$-\rho_0 LH\mathbf{v}_B \cdot \nabla q_B$	$\rho_0 Lw_E(q_{B+} - q_B)$	$L(F_q)_S$
0°, 95°W	−84	−84	124
2.5°N, 95°W	−222	−59	281

6. Conclusions

Using a simple bulk boundary layer model, we diagnose entrainment velocity, surface latent heat flux, and cumulus mass flux from monthly mean reanalysis data and the GLAS PBL depth. The entrainment velocity is similar to local velocities derived in other studies [e.g., DYCOMS II (Stevens et al. 2003a; Faloona et al. 2005 and DYCOMS (Kawa and Pearson 1989; WB04)] with increasing values westward in the southeast Pacific,

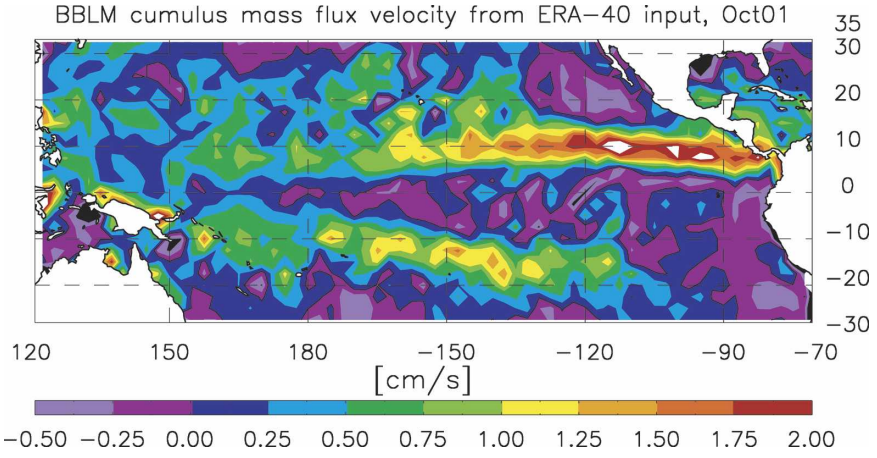

FIG. 4. Full solution from BBLM for cumulus mass flux velocity.

large values over the cold tongue to ITCZ transition zone, and large values in the northeast Pacific. Values range between 1 and 8 mm s^{-1} in most areas. The entrainment maximum along the Californian coast found in WB04 is missing in the BBLM field. A variety of factors may contribute to this discrepancy, including errors in the BBLM input data due to the underestimation of low cloud cover in ERA-40, as well as errors introduced by calculating gradients across the land–ocean boundary on a coarse grid. Also contributing may be a bias toward cloudy conditions in the WB04 estimate of the entrainment rate. The relative importance of the factors is, at this point, unknown.

The surface latent heat flux is much too large, particularly near the cold tongue. We find that the BBLM does not adequately represent the processes in this area in its present configuration. More vertical resolution is needed in the model and the input data to better represent the wind and PBL-top jumps of the moist conservative variables. Use of reanalysis data on model levels, for example, in conjunction with an explicit assumption of the vertical structure in the PBL (as done, e.g., in Betts et al. 1992; WB04) should improve the results, though at the cost of simplicity.

The cumulus mass flux, here defined as the mass flux through the trade inversion, is large where we would expect deep convection and strong mass convergence in the PBL. The velocity reaches its maximum of ~2 cm s^{-1} in the ITCZ, but is smaller in the warm pool and SPCZ (0.5 and 1.3 cm s^{-1}, respectively). The lack of a large convective mass flux in the warm pool may be related to the GLAS retrieval of the PBL depth. Since the PBL top is defined at the trade inversion, shallow cumuli contained entirely within the PBL do not contribute to the cumulus mass flux presented here. For future work, it might be beneficial to define the PBL top at cloud base, thus including contributions from all cumulus clouds to the mass flux and allowing a better comparison with existing studies of the cumulus mass flux in the trade wind regions. This is conditional on the availability of suitable data for cloud base height.

Overall, the GLAS-derived PBL depth is qualitatively in good agreement with observations of the trade inversion base. In some cases, GLAS appears to overestimate the PBL depth by ~200 m. It is hard to quantify how significant this difference is since in situ sonde measurements are compared to a 54-day GLAS mean of a different year. The fact that GLAS detects both cloudy and clear boundary layers may contribute to differences from sonde measurements.

The BBLM would benefit from improvements both in the model formulation and the input data, but manages to diagnose quite reasonable entrainment velocities. It provides insight how the contributions from local radiative forcing and advection vary in space. Alternative diagnostic strategies, such as the diagnosis of the moisture and temperature jumps, or the surface sensible heat flux could also be explored in future work.

Acknowledgments. This research was supported through the Pan American Climate Studies (PACS) of the National Oceanic and Atmospheric Administration under Contract NA17RJ1228 and by the National Science Foundation under Grant ATM-0415184. Our thanks to the reviewers, their helpful comments and constructive criticism are very much appreciated. Thanks also to Drs. Anton Beljaars and Martin Koehler for their help in understanding the ERA-40 reanalysis data. John Maurer from the National Snow and Ice Data Center and Dr. Steve Palm from the GLAS science team were of invaluable help in using and understanding the GLAS data.

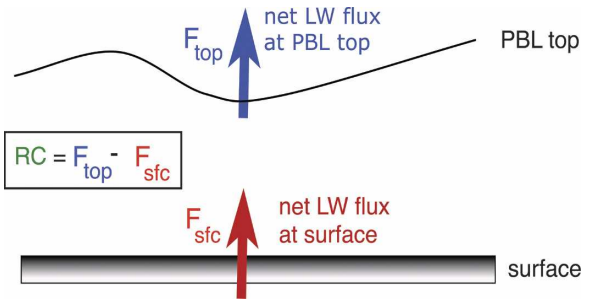

FIG. A1. Schematic of net longwave flux difference.

APPENDIX

The Representation of Radiative Cooling in the BBLM

To account for radiative cooling of the boundary layer, we approximate the difference of the net longwave (LW) flux between the boundary layer top and the surface (see Fig. A1) from ERA-40. ERA-40 supplies the net LW radiation on model levels. We calculate

$$\mathrm{RC}_{\mathrm{ERA}}(z) = F_{\mathrm{netLW}}(z) - F_{\mathrm{netLW}}(\mathrm{sfc}) \qquad \text{(A1)}$$

at each model level to create profiles of $\mathrm{RC}_{\mathrm{ERA}}(z)$. This is the vertically integrated flux divergence between the surface and the level in question. Figure A2 shows typical sample profiles for the deep convective region, the central Pacific, and the stratocumulus region.

Because each layer of the atmosphere cools radiatively, the increase of $\mathrm{RC}_{\mathrm{ERA}}$ with height is robust in the presence and absence of clouds. A limiting case is that of a stratocumulus-topped boundary layer in which the temperature of the earth's surface is similar to that of the cloud, and the surface upwelling and cloud downwelling LW radiation have similar magnitudes. In this case, the cooling is concentrated near the cloud top. Similarly, the upwelling and downwelling LW fluxes inside an optically thick cloud are approximately equal.

The presence of clouds in the monthly averaged sense is implicit in these profiles. The red profile in Fig. A2 (representing a stratocumulus case) shows a sharp increase in the net longwave flux difference between 500 and 1000 m, presumably where the cloud top is located. The black profile (a grid point in the warm pool area) does not show this sharp increase. The slopes above the expected boundary layer are also slightly different. Since the profiles represent a monthly mean, the slope of the red curve above ~1000 m is almost certainly a clear profile, whereas in the warm pool, we expect the curve to represent a time average of clear and cloudy conditions.

We pick the net longwave flux difference between the GLAS PBL and the surface at each grid point to represent the longwave radiative cooling experienced by the air mass contained in the PBL. The radiative cooling field thus obtained is shown in Fig. A3.

Alternatively, we could extrapolate the free-tropospheric part of the profile to the surface, and thus avoid

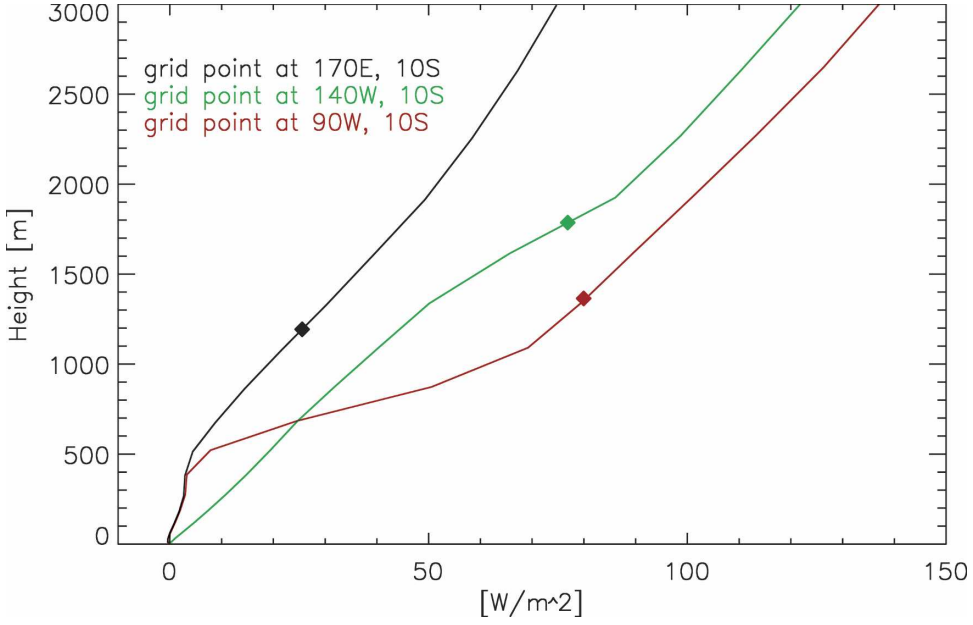

FIG. A2. Net longwave flux difference between model level height (ordinate) and surface. GLAS PBL top and corresponding radiative cooling marked by a diamond.

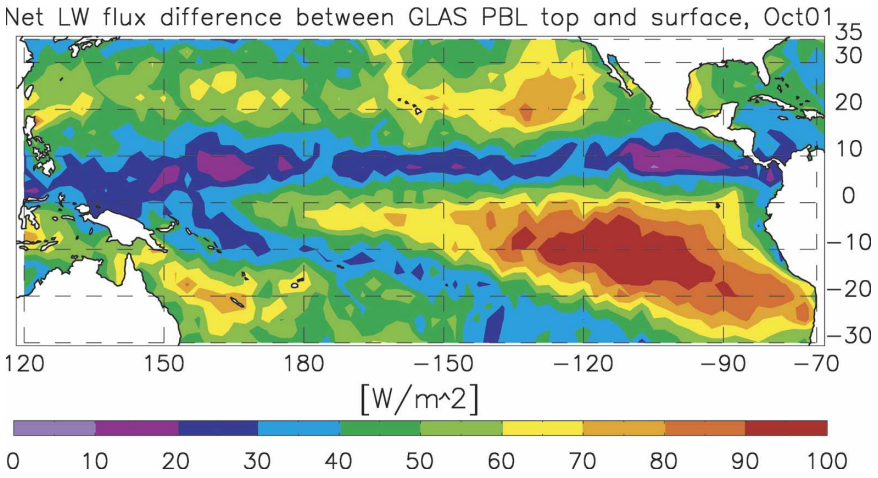

FIG. A3. Map of net longwave flux difference at each grid point, calculated from ERA-40 net longwave flux at the PBL-top height and the surface.

potential errors introduced where the GLAS cloud top is lower than the cloud top in ERA-40. The fields diagnosed with the alternative radiative cooling differ only insignificantly from the ones presented in this paper.

REFERENCES

Ahlgrimm, M., 2004: Diagnosing monthly mean boundary layer properties using a mixed-layer model. M.S. thesis, Dept. of Atmospheric Sciences, Colorado State University, 149 pp.

Arakawa, A., and W. H. Schubert, 1974: Interaction of a cumulus cloud ensemble with the large-scale environment, part I. *J. Atmos. Sci.,* **31,** 674–701.

Betts, A. K., P. Minnis, W. Ridgway, and D. F. Young, 1992: Integration of satellite and surface data using a radiative–convective oceanic boundary-layer model. *J. Appl. Meteor.,* **31,** 340–350.

Bretherton, C. S., and R. Pincus, 1995: Cloudiness and marine boundary layer dynamics in the ASTEX Lagrangian experiments. Part I: Synoptic setting and vertical structure. *J. Atmos. Sci.,* **52,** 2707–2723.

——, and Coauthors, 2004: The EPIC 2001 stratocumulus study. *Bull. Amer. Meteor. Soc.,* **85,** 967–977.

Chelton, D. B., A. M. Mestas-Nuñez, and M. H. Freilich, 1990: Global wind stress and Sverdrup circulation from the Seasat scatterometer. *J. Phys. Oceanogr.,* **20,** 1175–1205.

Chevallier, F., P. Bauer, G. Kelly, C. Jakob, and T. McNally, 2001: Model clouds over oceans as seen from space: Comparison with HIRS/2 and MSU radiances. *J. Climate,* **14,** 4216–4229.

Chou, S.-H., E. Nelkin, J. Ardizzone, R. M. Atlas, and C.-L. Shie, 2003: Surface turbulent heat and momentum fluxes over global oceans based on the Goddard Satellite Retrievals, version 2 (GSSTF2). *J. Climate,* **16,** 3256–3273.

Ciesielski, P. E., W. H. Schubert, and R. H. Johnson, 2001: Diurnal variability of the marine boundary layer during ASTEX. *J. Atmos. Sci.,* **58,** 2355–2376.

de Szoeke, S. P., and C. S. Bretherton, 2004: Quasi-Lagrangian large-eddy simulations of cross-equatorial flow in the east Pacific atmospheric boundary layer. *J. Atmos. Sci.,* **61,** 1837–1858.

——, ——, N. A. Bond, M. F. Cronin, and B. Morley, 2005: Epic 95°W observations of the eastern Pacific atmospheric boundary layer from the cold tongue to the ITCZ. *J. Atmos. Sci.*, **62,** 426–442.

Faloona, I., and Coauthors, 2005: Observations of entrainment in eastern Pacific marine stratocumulus using three conserved scalars. *J. Atmos. Sci.,* **62**, 3268–3285.

Firestone, J. K., and B. A. Albrecht, 1986: The structure of the atmospheric boundary layer in the central equatorial Pacific during January and February of FGGE. *Mon. Wea. Rev.,* **114,** 2219–2232.

Garreaud, R. D., J. Rutllant, J. Quintana, J. Carrasco, and P. Minnis, 2001: Cimar-5: A snapshot of the lower troposphere over the subtropical southeast Pacific. *Bull. Amer. Meteor. Soc.,* **82,** 2193–2207.

Hahn, C. J., and S. G. Warren, 1999: Extended edited synoptic cloud reports from ships and land stations over the globe, 1952–1996. Numerical Data Package NDP-026C, 71 pp. [Available from Carbon Dioxide Information Analysis Center, Oak Ridge National Laboratory, Oak Ridge, TN 37831–6335.]

Johnson, R. H., J. F. Bresch, P. E. Ciesielski, and W. A. Gallus, 1993: The TOGA/COARE atmospheric sounding array: Its performance and preliminary scientific results. Preprints, *20th Conf. on Hurricanes and Tropical Meteorology,* San Antonio, TX, Amer. Meteor. Soc., 1–4.

Kawa, S. R., and R. Pearson, 1989: An observational study of stratocumulus entrainment and thermodynamics. *J. Atmos. Sci.,* **46,** 2649–2661.

Kistler, R., and Coauthors, 2001: The NCEP-NCAR 50-year reanalysis: Monthly means CD–ROM and documentation. *Bull. Amer. Meteor. Soc.,* **82,** 247–267.

Kloesel, K. A., and B. A. Albrecht, 1989: Low-level inversions over the tropical Pacific—Thermodynamic structure of the boundary layer and the above-inversion moisture structure. *Mon. Wea. Rev.,* **117,** 87–101.

Lilly, D. K., 1968: Models of cloud-topped mixed layers under a strong inversion. *Quart. J. Roy. Meteor. Soc.,* **94,** 292–309.

McGauley, M., C. Zhang, and N. A. Bond, 2004: Large-scale char-

acteristics of the atmospheric boundary layer in the eastern Pacific cold tongue–ITCZ region. *J. Climate,* **17,** 3907–3920.

Neiburger, M., D. S. Johnson, and C. W. Chien, 1961: Studies of the structure of the atmosphere over the eastern Pacific Ocean in summer, I, The inversion over the eastern North Pacific Ocean. *Univ. Calif. Publ. Meteor.,* **1,** 1–94.

Norris, J. R., and C. B. Leovy, 1994: Interannual variability in stratiform cloudiness and sea surface temperature. *J. Climate,* **7,** 1915–1925.

Palm, S., W. Hart, and D. Hlavka, 2002: GLAS atmospheric data products. GLAS algorithm theoretical basis document, version 4.2, Science Systems and Applications, Inc., 137 pp.

Randall, D. A., Q. Shao, and M. Branson, 1998: Representation of clear and cloudy boundary layers in climate models. *Clear and Cloudy Boundary Layers,* A. A. M. Holtslag and P. G. Duynkerke, Eds., Royal Netherlands Academy of Arts and Science, 305–322.

Riehl, H., T. C. Yeh, J. S. Malkus, and N. E. LaSeur, 1951: The northeast trade of the Pacific Ocean. *Quart. J. Roy. Meteor. Soc.,* **77,** 598–626.

Rossow, W. B., and R. A. Schiffer, 1999: Advances in understanding clouds from ISCCP. *Bull. Amer. Meteor. Soc.,* **80,** 2261–2287.

Siebesma, A. P., and Coauthors, 2003: A large eddy simulation intercomparison study of shallow cumulus convection. *J. Atmos. Sci.,* **60,** 1201–1219.

Stevens, B., and Coauthors, 2001: Simulations of trade wind cumuli under a strong inversion. *J. Atmos. Sci.,* **58,** 1870–1891.

——, J. Duan, J. C. McWilliams, M. Munnich, and J. D. Neelin, 2002: Entrainment, Rayleigh friction, and boundary layer winds over the tropical Pacific. *J. Climate,* **15,** 30–44.

——, and Coauthors, 2003a: Dynamics and chemistry of marine stratocumulus—DYCOMS-II. *Bull. Amer. Meteor. Soc.,* **84,** 579–593.

——, and Coauthors, 2003b: On entrainment rates in nocturnal marine stratocumulus. *Quart. J. Roy. Meteor. Soc.,* **129,** 3469–3492.

Stull, R. B., 1988: *An Introduction to Boundary Layer Meteorology*. Kluwer Academic Publishers, 666 pp.

Troen, I., and L. Mahrt, 1986: A simple model of the atmospheric boundary layer: Sensitivity to surface evaporation. *Bound.-Layer Meteor.,* **37,** 129–148.

Winker, D. M., R. H. Couch, and M. P. McCormick, 1996: An overview of LITE: NASA's Lidar In-space Technology Experiment. *Proc. IEEE,* **84,** 1–17.

Wood, R., and C. S. Bretherton, 2004: Boundary layer depth, entrainment, and decoupling in the cloud-capped subtropical and tropical marine boundary layer. *J. Climate,* **17,** 3576–3588.

Woodruff, S. D., H. F. Diaz, J. D. Elms, and S. J. Worley, 1998: COADS Release 2 data and metadata enhancements for improvements of marine surface flux fields. *Phys. Chem. Earth,* **23,** 517–527.

Yanai, M., S. Esbensen, and J.-H. Chu, 1973: Determination of bulk properties of tropical cloud clusters from large-scale heat and moisture budgets. *J. Atmos. Sci.,* **30,** 611–627.

Zhang, C., M. McGauley, and N. A. Bond, 2004: Shallow meridional circulation in the tropical eastern Pacific. *J. Climate,* **17,** 133–139.

Zwally, H. J., and Coauthors, 2002: ICESat's laser measurements of polar ice, atmosphere, ocean, and land. *J. Geodyn.,* **34,** 405–445.

——, R. Schutz, S. Palm, W. Hart, S. Hlavka, J. Spinhirne, and E. Welton, 2005: GLAS/ICESat L2 global planetary boundary layer and elevated aerosol layer heights V019, 26 September to 18 November 2003. National Snow and Ice Data Center, digital media.